metals

Article

Fatigue Life Prediction Methodology of Hot Work Tool Steel Dies for High-Pressure Die Casting Based on Thermal Stress Analysis

Joeun Choi [1], Jongrak Choi [1], Kwangpyo Lee [2], Nahmkeon Hur [1] and Naksoo Kim [1,*]

1 Department of Mechanical Engineering, Sogang University, Seoul 04107, Korea
2 Technical Research Center, KONEC Co., Ltd., Seosan-si 32027, Korea
* Correspondence: nskim@sogang.ac.kr; Tel.: +82-2-705-8635

Abstract: High-pressure die casting (HPDC) can produce precise geometries in a highly productive manner. In this paper, the failure location and cycles were identified by analyzing the fatigue behavior of the die subjected to repeated thermal stress. An energy-based semi-empirical fatigue life prediction model was developed to handle the complex stress history. The proposed model utilizing mean stress, amplitudes of stress, and strain was calculated by one-way coupling numerical analysis of computational fluid dynamics (CFD) and finite element analysis (FEA). CFD temperature results of the die differed from the measured results by 2.19%. The maximum stress distribution obtained from FEA was consistent with the actual fracture location, demonstrating the reliability of the analytical model with a 2.27% average deviation between the experimental and simulation results. Furthermore, the model showed an excellent correlation coefficient of R^2 = 97.6%, and its accuracy was verified by comparing the calculated fatigue life to the actual die breakage results with an error of 20.6%. As a result, the proposed model is practical and can be adopted to estimate the fatigue life of hot work tool steels for various stress and temperature conditions.

Keywords: fatigue life prediction; hot work tool steel; high-pressure die casting; computational fluid dynamics; finite element analysis; thermal stress

Citation: Choi, J.; Choi, J.; Lee, K.; Hur, N.; Kim, N. Fatigue Life Prediction Methodology of Hot Work Tool Steel Dies for High-Pressure Die Casting Based on Thermal Stress Analysis. *Metals* **2022**, *12*, 1744. https://doi.org/10.3390/met12101744

Academic Editor: Filippo Berto

Received: 23 September 2022
Accepted: 14 October 2022
Published: 17 October 2022

1. Introduction

High-pressure die casting (HPDC) is a process wherein molten metal is injected inside the mold cavity at high speed and pressure conditions. This process has been widely utilized in the aerospace and automotive industries for its high productivity, product strength, corrosion resistance, and precise dimensional accuracy [1–3]. During HPDC, processes such as filling the chamber, solidifying, opening and closing, product removal, and spraying occur continuously [4]. Meanwhile, the die replacement procedure takes considerable time and increases production costs [5]. The reason is that the HPDC die manufacturing process requires high energy and many workforces due to being made of high-strength H13 hot work tool steel [6].

Therefore, thermal fatigue life prediction is essential to determine the replacement time of the die. Cumulative fatigue damage caused by thermal contraction and expansion of thermal stresses has a vital influence on die destruction. The thermal stress is caused by the uneven temperature distribution of the die due to an injection of high-temperature molten metal, product detachment, and repeated fast cooling via low-temperature coolant [7,8]. In particular, increased heat transfer due to the coolant flow channel reduces the process time by promoting rapid cooling; however, the temperature difference in the die rises, which is fatal to the thermal fatigue fracture [9]. The pressure and the temperature for evaluating the thermal stress can be accurately tracked by employing load cells and thermocouples. Additionally, the molten metal flow remains constant for each cycle, causing the temperature field to converge [10,11]. Therefore, it is unnecessary to analyze the thermal stress at every HPDC cycle [12,13].

Many studies have confirmed the temperature effect on thermal fatigue behavior through experiments or numerical analysis [14–20]. Wei et al. [21] suggested a methodology for considering thermal stress within Abaqus software by employing a simplified die casting model. In addition, Klobčar et al. [15] evaluated the strength of the die material against thermal stress through experiments in which the die specimen was repeatedly immersed in water and aluminum molten metal. Meanwhile, the studies mentioned above have limitations arising from their difficulty in simulating the actual HPDC and its complicated experiments confined to a specimen.

Concerning fatigue analysis, typical conventional models have been suggested by Goodman [22], Smith–Watson–Topper (SWT) [23], Walker [24], and Coffin–Manson [25,26]. These models have been introduced to predict the fatigue life of materials via maximum and minimum stress or strain. Meanwhile, the Rainflow counting method, which converts various loading sequences into constant stress amplitude, has also been proposed by Matsuishi and Endo [27]. Nevertheless, stress or strain history under the operating environment of products is highly complex, making it challenging to apply these fatigue life prediction models.

For this reason, many studies have been conducted to describe fatigue behavior in complex stress states by adopting various methods [28–35]. For instance, Choi et al. [29] proposed a semi-empirical model based on the specimen angles and strain amplitude, representing the nonlinear anisotropic behavior. Meanwhile, Lu et al. [16] developed a thermal fatigue model by utilizing the relationship between the thermal plastic strain and the temperature change. The temperature change is the difference between the initial and final temperature in the thermal fatigue test of the simple plate and dies insert samples. The proposed model was improved using the temperature at the point where the plastic strain was rapidly induced.

As summarized so far, the fatigue behavior of the die material can be described through a semi-empirical fatigue life prediction model. Various attempts have been made to predict the fatigue life of the die casting die in consideration of thermal stress via the temperature difference term and experimental results [16,36–38]. However, there appear to be no prior studies that predict fatigue life of the die under constantly changing thermal stress and complex stress states by utilizing the relationship between maximum and minimum average stress–strain. In addition, many studies have been conducted to attempt thermal and structural analysis individually; still, the successful development of one-way coupled numerical analysis has yet to be achieved.

For these reasons, a thermofluid analysis model was developed considering the temperature change in the die in the actual HPDC process. The simulation was conducted for 20 repeated cycles to obtain a converged periodic temperature field throughout all computational domains. Furthermore, a one-way co-simulation of structural analysis was carried out based on the temperature result of computational fluid dynamics (CFD). Thermal stress–strain of finite element analysis (FEA) was evaluated utilizing the quasi-steady-state assumption based on the instantaneous temperature distribution.

For determining the temperature effects on the AISI H13 hot work tool steel, the flow stress model and temperature-dependent coefficients were chosen and adopted for the numerical simulations. The Johnson–Cook flow stress model, comprising the mechanical and thermal properties, was selected to define a relationship between thermal strain and temperature [39–42]. The model parameters were determined using the tensile experiment results at different experimental temperatures and employed in an FEA model. The low-cycle fatigue life simulation results were verified by comparing to the experimental results, which show good agreement with the actual crack positions.

In addition, fatigue tests were performed with various stress and temperature conditions to predict the fatigue life of the HPDC die. As a result, a semi-empirical model enabling the prediction of the fatigue failure life under exposure to thermal stress was proposed based on simulation and experimental results. The proposed model is a strain–stress-based energy function in a power-law form. The energy function was calculated utilizing the maximum and minimum stress–strain obtained from the die, and the fatigue life can be predicted without stress–strain change history. Moreover, by conducting three case studies with different coolant passages, the best design capable of improving the fatigue life of the die was evaluated. As the results of this research, designers can predict vulnerabilities in advance and compare the fatigue life considering the effect of thermal stress.

2. Materials and Methods

The fatigue life prediction of the die subjected to thermal stress at various temperatures was performed through the procedure shown in Figure 1. First, static and fatigue experiments were carried out utilizing machined uniaxial and notch specimens to appraise the mechanical properties under various load conditions. Additionally, the temperature and pressure on the dies were measured with a thermocouple and load cell. Arduino Uno collects the measurement data every 0.31 s.

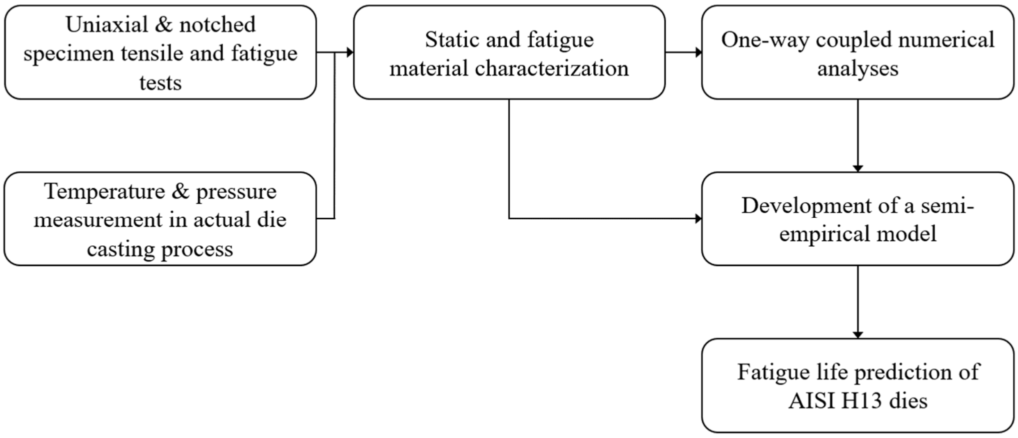

Figure 1. Fatigue life prediction procedures of AISI H13 die casting die.

Secondly, the material coefficients adopted for numerical analysis were determined by the stress–strain curves obtained from the tensile tests. Furthermore, the boundary conditions of one-way coupled numerical analysis combining CFD and FEA were defined using measured temperature and pressure data. The thermal stress could be accurately evaluated through the developed simulation by mapping the temperature distribution to structural analysis. Finally, the semi-empirical model utilizing energy function was developed by assessing the effects of thermal stress. The strain and stress values in the hysteresis loop of each fatigue test condition were extracted from the FEA results. The acquired values were used as input to the semi-empirical model, allowing prediction of the fatigue life.

2.1. Materials and Experimental Methods

Heat-treated AISI H13 was selected as a die material for the HPDC process. Table 1 shows the chemical composition of heat-treated AISI H13, and the physical and thermal properties are reported in Table 2. In addition, uniaxial tensile and fatigue tests were conducted to characterize static and fatigue behavior. The dimensions of the tensile and fatigue specimens were determined considering the ASTM E8 and E466 standards and the grip part of the test equipment, thereby facilitating specimen production. The ASTM E8 standard has a gauge length equivalent to four times the diameter of the central region for small round bar specimens. Therefore, the center diameter was set to 5 mm, and the gauge length was set to 20 mm following the standard. In addition, depending on the ASTM 466, the grip part diameter was defined as 12 mm, 1.5 times or more than the center diameter. The fillet radius was set to be 30 mm, smaller than the proposed standard of 40 mm, in consideration of the short fixed part of the experimental equipment [43,44]. The specimens were machined in three different shapes: uniaxial and two types of notched shapes. The experiments were carried out at temperatures of 20, 300, and 500 °C using an MTS Landmark servo-hydraulic test system at 50% relative humidity. The dimensions of the specimens and the testing machine can be seen in Figure 2.

Table 1. The chemical composition of AISI H13 hot work tool steel (wt%).

Cr	Mo	Si	V	C	Ni	Cu	Mn	P	S
4.7–5.5	1.1–1.8	0.8–1.2	0.8–1.2	0.3–0.5	0.3	0.25	0.2–0.5	0.03	0.03

Table 2. The physical and thermal properties of AISI H13 hot work tool steel.

Density (g/cm^3)	Specific Heat Capacity (J/g·°C)	Thermal Conductivity (W/m·K)
7.80	0.46	24.3

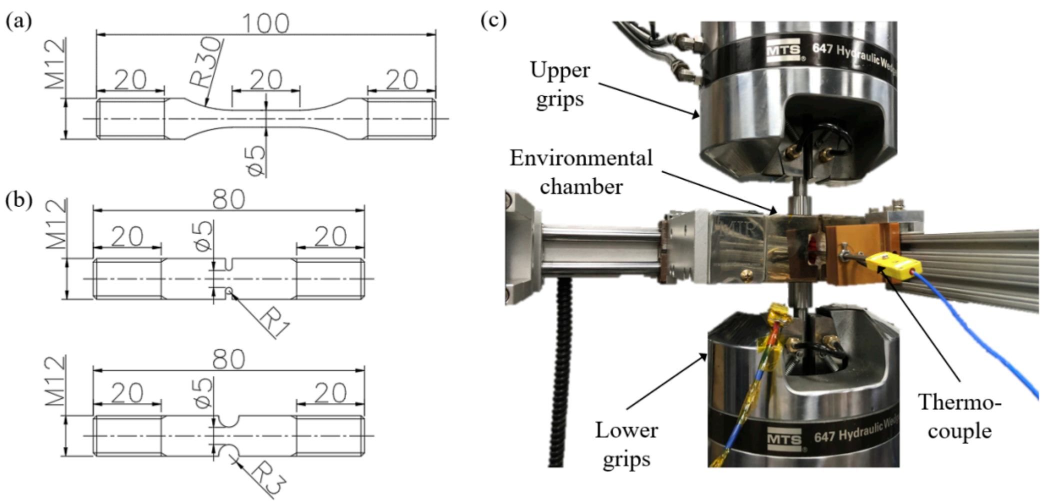

Figure 2. Specifications of uniaxial and notched specimens and an environment of testing machine setup. All dimensions are denoted in mm. (**a**) Dimensions of uniaxial specimen designed, based on the ASTM E8 and ASTM E466 standards. (**b**) A notched specimen dimensions. (**c**) The experimental setting for static and fatigue tests of MTS Landmark servo-hydraulic test system.

The uniaxial tensile tests were conducted at 50 mm/min tensile speed to evaluate the static mechanical properties. The attained stress–strain curves were utilized to determine Johnson–Cook flow stress model parameters, as described in Section 2.2.2. Furthermore, the fatigue experiments were set up by a stress ratio (R = 0.05) and maximum stress, using tension–tension loading load-controlled conditions. The stress ratio is the minimum stress divided by the maximum stress. The fatigue test frequency was 1 Hz, and experiments were carried out at the same temperatures as used for the static tests.

2.2. Numerical Analysis Methodology

The die is continuously damaged by thermal–mechanical stress due to repeated thermal expansion and contraction in the process cycle. This phenomenon is intensified due to the temperature difference between the molten metal and the coolant. Therefore, it is essential to calculate the thermal–mechanical stress field precisely. For these reasons, the one-way co-simulation of the CFD and the FEA was developed. The procedure for the proposed one-way co-simulation is summarized in Figure 3.

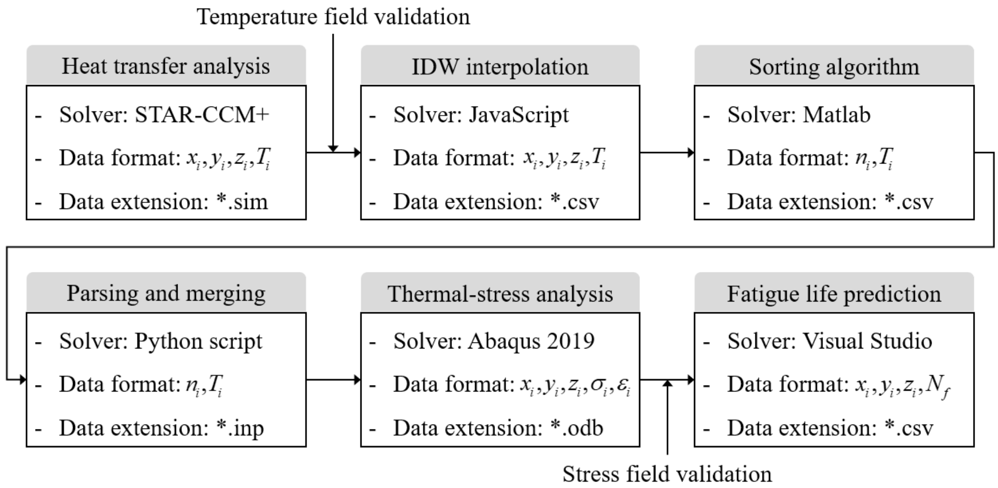

Figure 3. The procedure for one-way coupling fluid–structure interaction simulations for fatigue life prediction of the die. * indicates the name of the data file.

First, the temperature distribution of the solid mesh was obtained by CFD. The temperature data are in the polyhedral centroid mesh because CFD uses a finite volume method (FVM) solver. For this reason, transient CFD results were interpolated to nodes by the inverse distance weighted (IDW) method. Next, the storage data in the FVM were changed to suit the FEA through the sorting algorithm. Afterward, the input files of the FEA were created by parsing and merging the sorted data. Finally, the thermal stress was calculated, and the fatigue life of the die could be predicted. Additionally, all procedures were verified by comparing the simulation results with the actual HPDC process.

2.2.1. Thermofluid Analysis

A three-dimensional CFD with a conjugate heat transfer model was required to analyze the solid part's spatial and temporal temperature distribution. This study considered the effect of the coolant flow on local heat transfer by the passage. The flow inside the coolant passage was numerically simulated using continuity and momentum equations, as follows:

$$\frac{\partial V_i}{\partial x_j} = 0 \tag{1}$$

$$\frac{\partial (V_j V_i)}{\partial x_j} = -\frac{1}{\rho}\frac{\partial p}{\partial x_i} + \frac{\partial}{\partial x_j}\left[\nu\left(\frac{\partial V_i}{\partial x_j} + \frac{\partial V_j}{\partial x_i}\right)\right] \tag{2}$$

Here x_i is the cartesian coordinate, V_i the velocity component, ρ the fluid density, p the pressure, and ν the kinematic viscosity. The coolant rejects the heat from the surface of the passage by forced convection heat transfer. Since the coolant is liquid and the average velocity through the path is low, an incompressible flow is assumed. The gravitational acceleration is ignored because the die part is not large enough to consider the hydraulic pressure.

The unsteady-state simulation is modeled using appropriate boundary conditions based on the complete HPDC process. The HPDC occurs in five steps, as shown in Figure 4: mold filling, the opening of the movable die, part removal, coolant spraying, and closing of the movable die. The thermal flow analysis boundary conditions were divided according to the process chain. When the die was opened and sprayed, a convective heat transfer coefficient of air and coolant was given, and the measured temperature was applied when in contact with the molten metal. Numerical analysis was conducted without modeling the spraying tool, assuming homogeneous distribution of the air and coolant. This assumption was verified by comparing the measured temperature results of the infrared camera to the simulation temperature.

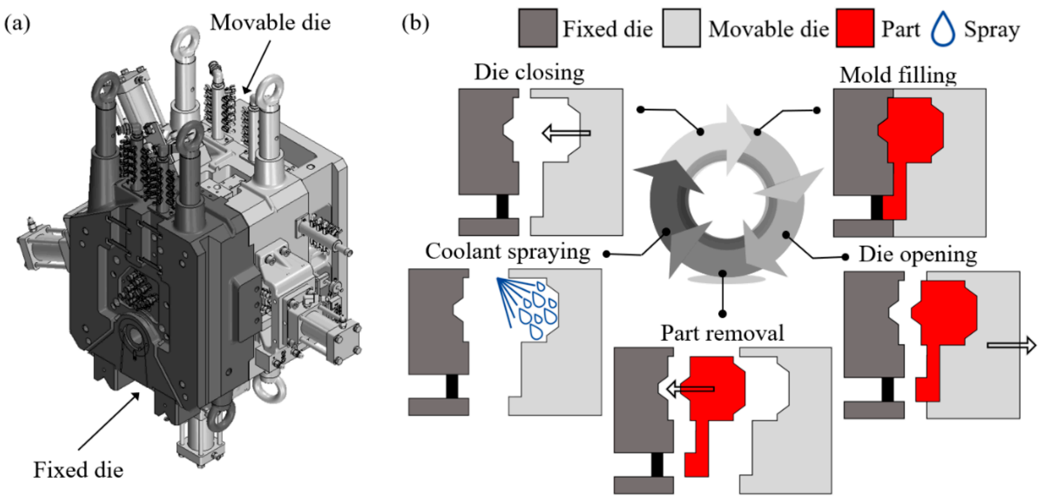

Figure 4. Die casting process overview. (**a**) Movable and fixed die. (**b**) The one-cycle process chain of HPDC.

Fatal breakage arises on the distributor of the movable die, where temperature differences occur significantly. Therefore, the simulation area was selected as a distributor and a peripheral die. This modeling significantly contributed to the reduction in the analysis time by excluding the unnecessary area. Temperature and pressure data measured by the thermocouple and load cell were applied as boundary conditions for the distributor of the movable die. The numerical analysis domain and the data measurement method are shown in Figure 5.

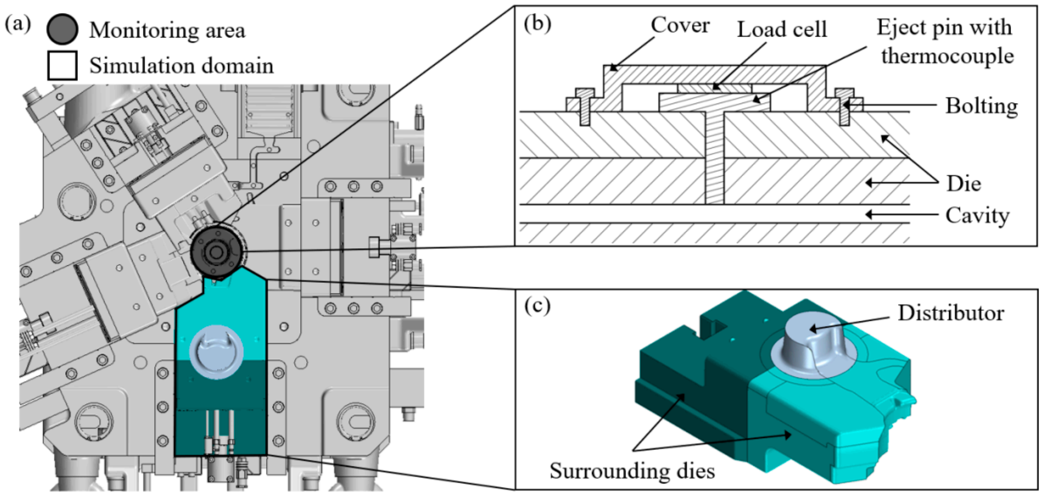

Figure 5. Numerical analysis parts and the data measuring method. (**a**) The locations of the monitoring areas and analysis region. (**b**) The temperature and pressure measuring setup. (**c**) Numerical analysis model for distributor and the surrounding dies.

The thermofluid analysis was performed using STAR-CCM+ commercial software, which was used to obtain periodic temperature history. The simulation was continuously simulated over 20 cycles to obtain the stabilized temperature field. Convection and conduction heat transfer, and adiabatic boundary conditions were defined. Heat transfer coefficients (100 and 10,000 $W/m^2{\cdot}K$) were adopted for considering the forced convection in the blowing and spraying processes for air and coolant, respectively. In addition, heat transfer analysis was performed through thermal resistance modeling between fluid molten metal and solid die. The boundary condition between solid and solid was given in the solid cast state before 480 °C. The resistance between fluid and solid was applied in the liquid cast state at a temperature above that. The heat transfer and thermal resistance coefficient according to the temperature are shown in Table 3. The boundary conditions between the copper plating and the AISI H13 are also granted. All the thermofluid boundary conditions are summarized in Figure 6.

Table 3. The heat transfer coefficients and the thermal contact resistance considering solid and liquid cast temperatures.

Temperature (°C)	Heat Transfer Coefficient ($W/m^2 \cdot K$)	Thermal Contact Resistance (R'') ($\times 10^{-5}$/K)
479	400	250
579	17,000	5.88
600	38,000	2.63
620	42,000	2.38
700	42,000	2.38

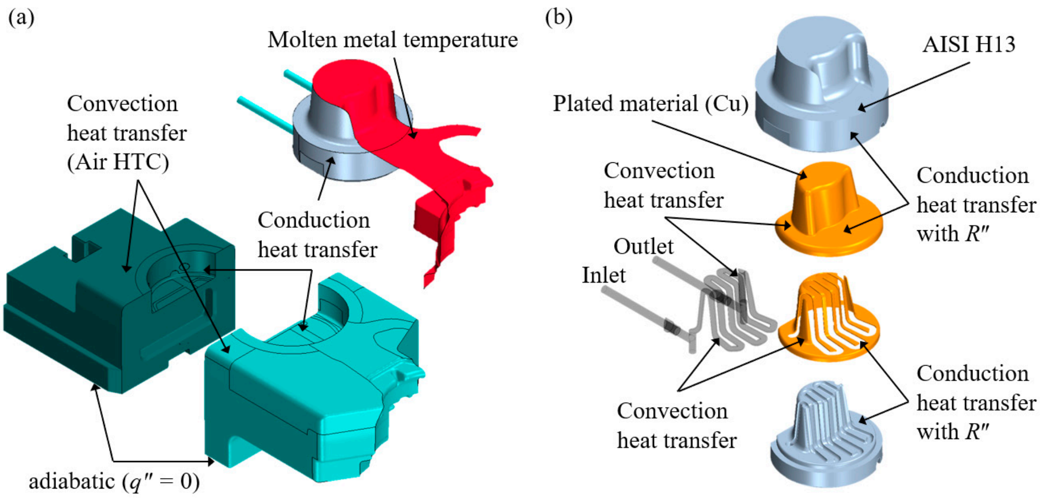

Figure 6. Thermal boundary conditions for thermofluid analysis. (**a**) Boundary conditions between the entire simulation domains. (**b**) Boundary conditions inside the combined different materials distributor (silver: AISI H13, yellow: Cu).

2.2.2. Thermostress Analysis

The thermal stress was evaluated by FEA, utilizing the commercial software Abaqus 2019. The difference in the thermal expansion between AISI H13 and copper induces thermal stress. The linear thermal expansion coefficient α_i is selected to acquire the thermal strain. The thermal strain difference between the current and initial temperatures can be gained by the increment concept in Abaqus/Standard. The α_i of copper and AISI H13 hot work tool steel material according to temperature were applied to simulate the temperature-dependent behavior, as shown in Table 4.

$$\Delta\varepsilon_i^{th} = \varepsilon_i^{th} - \varepsilon_{init}^{th} = \alpha_i\left(T_i, f_\beta^i\right)(T_i - T_0) - \alpha_{init}(T_{init} - T_0) \quad (3)$$

$$\alpha_i \equiv \frac{1}{L}\frac{dL}{dT} \cong \frac{\varepsilon_i^{th} - \varepsilon_0^{th}}{T_i - T_0} \quad (4)$$

Table 4. The thermal expansion coefficients of copper and AISI H13 hot work tool steel.

Material	**Temperature (°C)**	**Thermal Expansion Coefficient (α_i) ($\times 10^{-6}$/°C)**
Copper	25	16.0
	650	20.0
AISI H13 hot work tool steel	100	10.4
	250	11.5
	400	12.6
	550	13.0

The temperature distributions were interpolated to match the computational points of FVM and FEM by the IDW method. The distance between the target and nearby points is calculated and multiplied by the weight function. Interpolated values are obtained utilizing Java Script. The definition of thermal expansion and IDW are shown in Figure 7.

$$d_i(\mathbf{x}, \mathbf{x}_i) = \sqrt{(x - x_i)^2 + (y - y_i)^2 + (z - z_i)^2} \tag{5}$$

$$w_i(\mathbf{x}) = \frac{1}{d_i(\mathbf{x}, \mathbf{x}_i)^p} \tag{6}$$

$$\phi(\mathbf{x}) = \begin{cases} \dfrac{\sum_i^N w_i(\mathbf{x})\phi_i}{\sum_i^N w_i(\mathbf{x})} & d_i(\mathbf{x}, \mathbf{x}_i) \neq 0 \\ \phi_i & d_i(\mathbf{x}, \mathbf{x}_i) = 0 \end{cases} \tag{7}$$

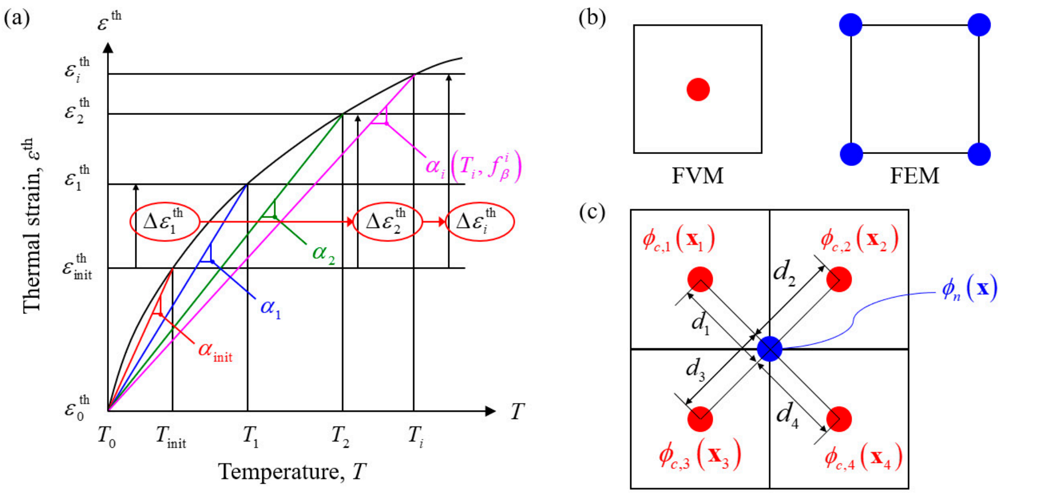

Figure 7. Definition of thermal expansion and the IDW method. (**a**) Determining thermal strain by the incremental concept. (**b**) Computational points of FVM (**left**) and FEM (**right**). (**c**) Distance between FVM and FEM points in IDW method.

The interpolated values are stored with the coordinate systems. Next, the data are sorted, and the coordinate systems are matched to their nodal points using the Matlab sorting algorithm. Then, the node numbers with temperature data are parsed and merged. Finally, the modified values are written to Abaqus input. The parsing, combining, and writing steps are conducted with a Python script.

Thermal stress–strain values are evaluated using quasi-steady-state assumptions based on instantaneous temperature distribution. The stress–strain relationship is defined as the shear stress and the temperature difference:

$$\sigma_{ij} = 2G\left[\frac{1}{2}(u_{ij} + u_{ji}) - \alpha\Delta T\delta_{ij}\right] + \overline{\lambda}u_{kk}\delta_{ij} \tag{8}$$

where σ, G, u_i, a, ΔT, and $\overline{\lambda}$ refer to, respectively, a stress component, the shear modulus, the displacement component, the linear thermal expansion coefficient, a temperature difference, and the Lamé constant. The Johnson–Cook model is selected as the flow stress model. The Johnson–Cook model is one of the models that can accurately simulate the temperature-dependent flow stress of a hot work tool steel material.

$$\sigma = (A + B\varepsilon^n)\left(1 + C\ln\dot{\varepsilon}^*\right)(1 - T^{*m}) \tag{9}$$

$\dot{\varepsilon}^*$ is the dimensionless effective strain rate ($\dot{\varepsilon}^* = \dot{\varepsilon}/\dot{\varepsilon}_0$), and T^{*m} the dimensionless temperature ($T^{*m} = (T - T_0)/(T_{melt} - T_0)$), where T_0 is a reference temperature and T_{melt} the melting point. A, B, C, n, and m are Johnson-Cook model parameters. Attained stress–strain curves of tensile experiments are used to determine the Johnson-Cook model parameters.

The analysis model has 2,083,878 four-node tetrahedral elements (C3D4). The bottom surface attached to the rear die has fixed boundary conditions in the x, y, and z directions. In addition, the surface where each die connected to another is restricted to surface-to-surface contact constraints. The boundary conditions applied to the thermal stress analysis are summarized in Figure 8.

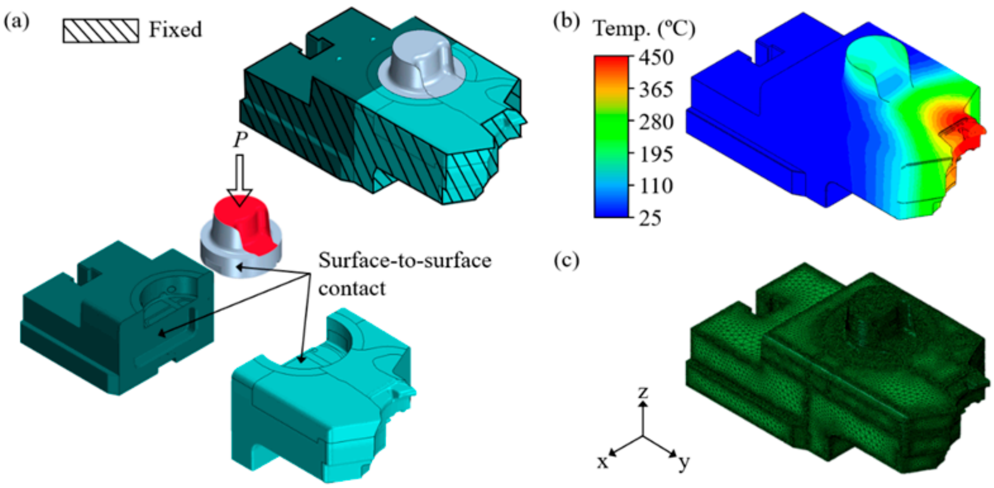

Figure 8. Boundary conditions and simulation model of thermal stress analysis. (**a**) Boundary conditions with a fixed, surface-to-surface contact, and pressure constraints. (**b**) Interpolated temperature-distribution boundary conditions. (**c**) Analysis model with generated mesh.

2.3. Fatigue Life Prediction Model

The semi-empirical fatigue life prediction model of AISI H13 die is proposed to manage the effects of repeated thermal stress. The developed model starts with the Manson–Coffin strain-based fatigue life model [26].

$$f(\varepsilon) = \frac{\left(\varepsilon_{p,\,\max} - \varepsilon_{p,\,\min}\right)}{2} = \Delta\varepsilon_p = A\left(N_f\right)^c \tag{10}$$

In the Manson-Coffin model, the fatigue life can be estimated by the total plastic strain amplitude $\Delta\varepsilon_p$ with two material coefficients A and c. Manson-Coffin-Basquin model appended elastic deformation and linked the relationship to the failure stress.

$$\varepsilon_{\mathrm{a,t}} = \varepsilon_{\mathrm{a,e}} + \varepsilon_{\mathrm{a,p}} = \frac{\sigma'_f}{E}\left(2N_f\right)^b + \varepsilon'_f(2N_{\mathrm{f}})^c \quad (11)$$

The total strain amplitude $\varepsilon_{\mathrm{a,t}}$ is expressed as the sum of the elastic and the plastic strain amplitude, $\varepsilon_{\mathrm{a,e}}$ and $\varepsilon_{\mathrm{a,p}}$, respectively. Furthermore, the elastic strain amplitude represents true fracture stress σ'_f, Young's modulus E, and the cycles to failure N_f. In addition, the plastic strain amplitude is described as the true fracture strain $\varepsilon'_{\mathrm{f}}$ and the failure cycle. Although the Manson-Coffin-Basquin equation has been used in numerous studies, it has difficulty reflecting the repeated effect of thermal stress.

In addition, when the mean stress in the actual design is included, the material becomes more vulnerable to fatigue. Substituting this phenomenon to the Basquin model, the fatigue life decreases when the mean stress increases.

$$\frac{\Delta\varepsilon^{\mathrm{tot}}}{2} \approx \frac{\left(\sigma'_f - \sigma_m\right)\left(2N_f\right)^b}{E} + \varepsilon'_f\left(2N_f\right)^c \quad (12)$$

It can be seen that the mean stress must be compensated through the strain amplitude to keep the lifetime the same. When this is summarized from the stress perspective, Goodman's rule is derived.

$$\frac{\Delta\sigma_{\sigma m}}{2} \approx \frac{\Delta\sigma\left(\sigma'_f - \sigma_m\right)}{2\sigma'_f} \quad (13)$$

This study combines the abovementioned models to develop a model that can consider the effects of repeated thermal stress and temperature.

$$f(\varepsilon,\, \sigma) = \left(\frac{\varepsilon_{\max} - \varepsilon_{\min}}{2\varepsilon_f}\right)\left(\frac{\sigma_{\max} - \sigma_{\min}}{2\sigma_f}\right)\left(\frac{\sigma_{\max} + \sigma_{\min}}{2\sigma_f}\right) = \frac{\Delta\varepsilon \cdot \Delta\sigma \cdot \sigma_m}{\underbrace{\varepsilon_f \sigma_f^2}_{\text{material characteristics}}} = A\left(N_f\right)^c \quad (14)$$

The denominators of all terms consist of the uniaxial tensile fracture strain and stress (ε_f and σ_f). Subsequently, the denominators of the entire model are determined by material characteristics. The first term may assess the effects of temperature distribution in the process. Since the thermal strain depends on the temperature change, the fatigue fracture can be predicted efficiently without using the temperature term directly. The maximum and minimum difference in the strain, $\varepsilon_{\max}$ and $\varepsilon_{\min}$, allows the calculation of the die's damage at the highest and lowest temperatures. As a result, there is an advantage in that it is not necessary to evaluate the constantly changing temperature, thus simplifying the otherwise complex calculation.

The second and third terms consider the von Mises equivalent stress. The second term involves the impact of thermal stress through the difference between maximum and minimum stresses ($\sigma_{\max}$ and $\sigma_{\min}$). In addition, by adding a third term for mean stress, complex stress states can be considered. A and c are material coefficients calculated in exponential form based on the fatigue experiments. A model was developed to maximize the influence of thermal stress by including the stress-related term twice.

3. Results

3.1. Static and Fatigue Mechanical Properties

The load–stroke and the true stress–strain curves relevant for the unnotched and two types of notched specimens are reported in Figures 9 and 10, respectively. The effects at three different environmental temperatures (20, 300, and 500 °C) can be confirmed. As the experiment operating temperature increases, AISI H13 steel significantly reduces yield and tensile strength. In addition, the different triaxialities caused by the three dimensions of specimens (R = 0, 1, and 3 mm) changed the fracture displacements. When a material is subjected to a complex stress state due to increased triaxiality, fracture occurs more quickly, reducing fracture strain and stress.

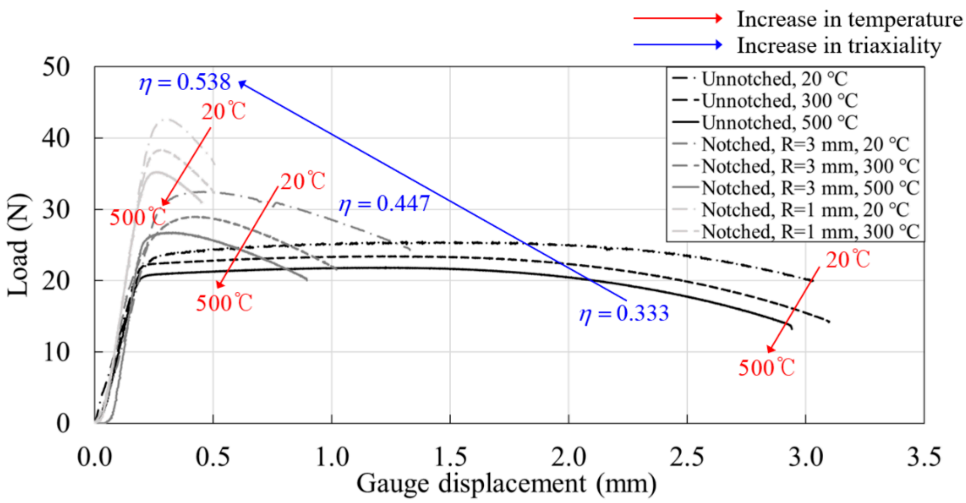

Figure 9. Load–displacement curves of the tensile experiments for the unnotched and notched specimens at 20, 300, and 500 °C environmental temperatures.

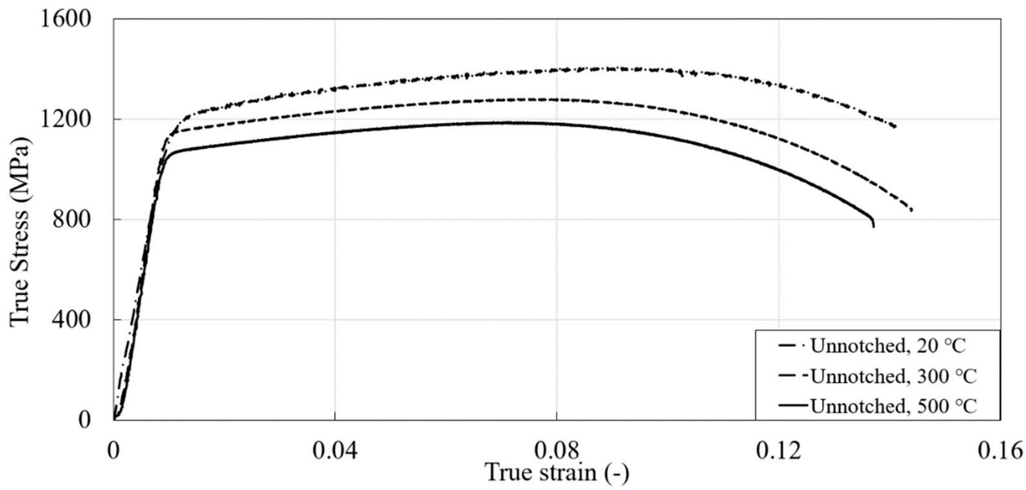

Figure 10. True stress and strain curves of the AISI H13 material for 20, 300, and 500 °C temperatures.

Three repeatability tests were carried out, and the average results were employed. The Johnson–Cook flow stress model coefficients were determined through the L-BFGS-B algorithm implemented in the Python script by comparing the load–displacement curves between the experimental and FEA results, as shown in Table 5.

Table 5. The Johnson–Cook flow stress model parameters of AISI H13 determined by tensile tests.

Parameter	*A* (MPa)	*B* (MPa)	*C* (-)	*n* (-)	*m* (-)
Value	560	5.293	0.031	0.2789	0.1141

Failure cycles from 10^2 to 10^5 were considered for all temperatures and triaxiality. The true stress and strain associated with the unnotched specimens were calculated immediately. The data of notched specimens could not be obtained directly due to the complex geometries; hence the stress and strain were gathered through FEA results. All values were acquired from the last stabilization cycle. The difference between the selected and fracture cycle was less than 5% in terms of maximum and minimum displacement. All fatigue test conditions, fracture cycles, and the energy function values worked out by the proposed semi-empirical model are presented in Table 6. The developed model constants, A and c, are equal to 0.05762 and −0.2143, showing high accuracy with the 0.976 correlation factor. The regression line, calculated by the obtained model parameters, and an energy function vs. the number of failure cycles are shown in Figure 11.

Table 6. Summary of fatigue experiments on the uniaxial and notched specimens.

Geometry	Triaxiality (η)	Temp. (°C)	ε_{max} (-)	ε_{min} (-)	$(\sigma_{vM})_{max}$ (MPa)	$(\sigma_{vM})_{min}$ (MPa)	N_f (Cycles)	Energy Function (-)
Unnotched specimen	0.333	20	0.013	0.001	1200	60	1373	0.0119
			0.010	0.000	1100	55	11,588	0.0074
			0.008	0.000	1000	50	47,340	0.0052
		300	0.009	0.001	1100	55	1215	0.0123
			0.008	0.001	1000	50	8164	0.0087
			0.007	0.001	900	45	20,690	0.0064
		500	0.009	0.002	1000	50	2340	0.0112
			0.008	0.001	950	48	3835	0.0094
			0.008	0.001	900	45	10,873	0.0080
Notched specimen (R = 3 mm)	0.447	20	0.011	0.001	1200	60	949	0.0139
			0.008	0.000	1100	55	4635	0.0086
			0.007	0.000	1000	50	33,955	0.0061
		300	0.008	0.001	1100	55	787	0.0140
			0.007	0.001	1000	50	3308	0.0107
			0.006	0.001	900	45	44,955	0.0056
		500	0.007	0.002	1000	50	1093	0.0126
			0.007	0.001	950	48	2862	0.0106
			0.006	0.001	900	45	5580	0.0090
Notched specimen (R = 1 mm)	0.538	20	0.009	0.000	1200	60	470	0.0154
			0.007	0.000	1100	55	1031	0.0134
			0.006	0.000	1000	50	5100	0.0101
		300	0.006	0.001	1100	55	413	0.0160
			0.005	0.001	1000	50	1990	0.0112
			0.005	0.001	900	45	11,980	0.0082
		500	0.006	0.001	1000	50	488	0.0150
			0.005	0.001	950	48	910	0.0126
			0.005	0.001	900	45	3980	0.0106

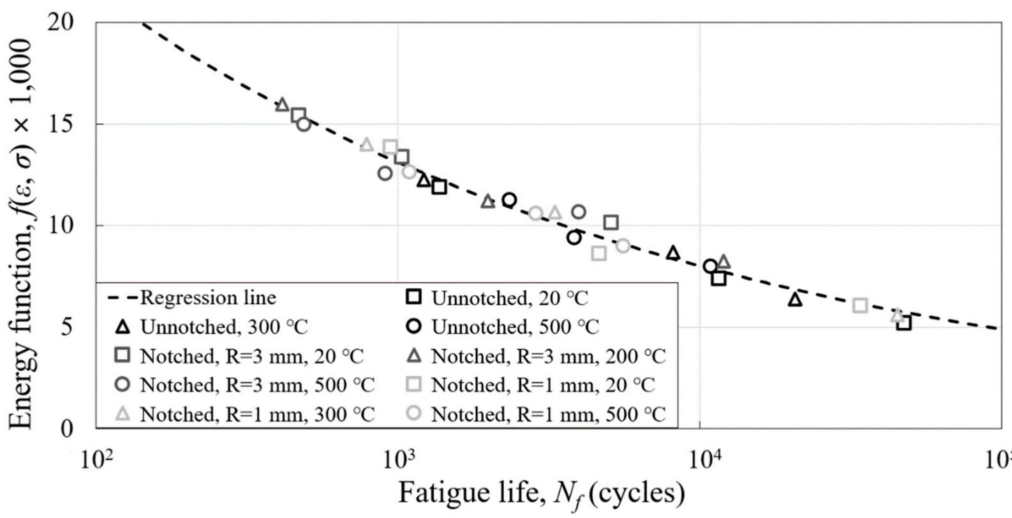

Figure 11. Energy function vs. fatigue life curve of the AISI H13 hot work tool steel (log–linear scale).

3.2. Numerical Analysis Results

The proposed one-way coupled method was used to evaluate the molten metal and cooling water's temperature distribution and thermal stress. Verification was performed for each analysis stage. First, the thermofluid analysis was performed 20 times to consider that the die was heated due to molten metal from atmospheric temperature. The temperature convergence results at the die and the outlet of the coolant are shown in Figure 12. After convergence, the simulation was conducted for one more cycle and utilized for thermal stress analysis.

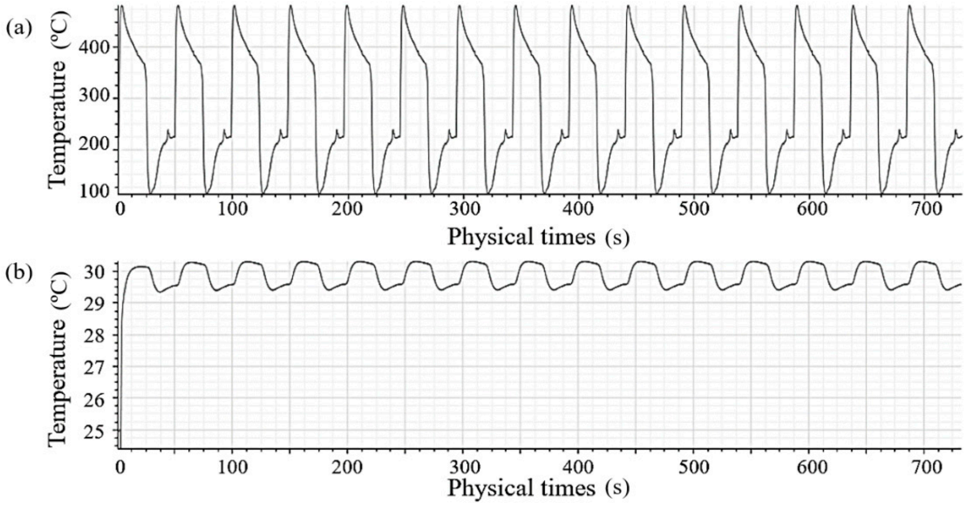

Figure 12. CFD results of the die casting process cycle through time. (**a**) Temperature convergence at the thermocouple measurement position in the die. (**b**) Temperature convergence at the coolant outlet.

The thermal analysis compared the temperature between the infrared camera measurement and the simulation results at the same point of the die. The deviation of the two measured results was 2.19%, confirming the rationality of the adopted heat transfer coefficient and boundary conditions (Figure 13). Finally, the verified CFD temperature calculation results were mapped to FEA. The temperature distribution comparison for the thermal and structural analyses is shown in Figure 14.

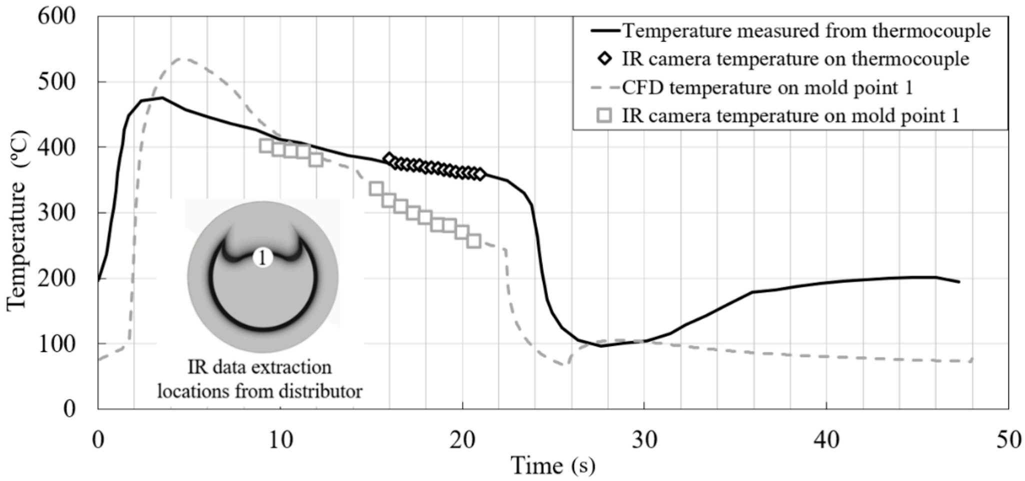

Figure 13. Measured and simulated temperatures on the die during the one-cycle HPDC.

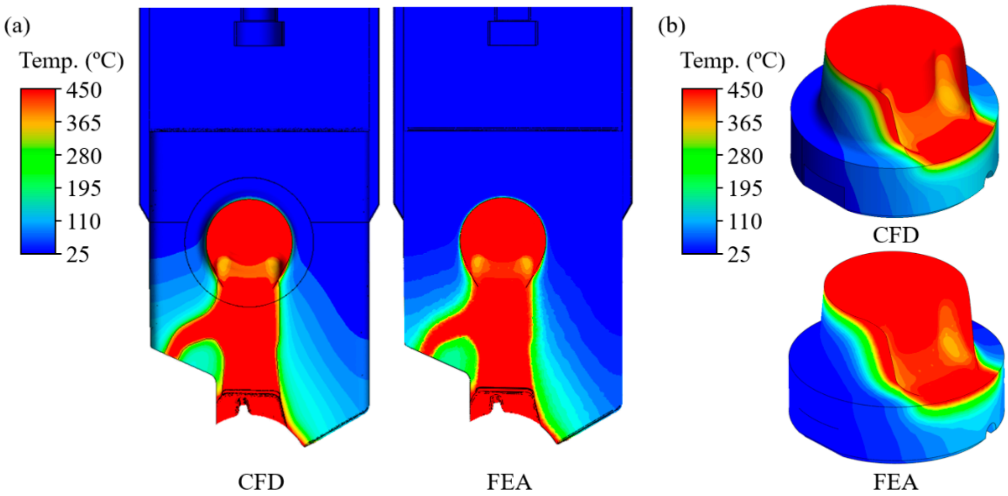

Figure 14. Temperature distribution of thermofluid analysis and IDW interpolation. (**a**) Temperature from the top view of the entire analysis model (**left**: CFD, **right**: FEA). (**b**) Temperature from an isometric perspective of the distributor (**top**: CFD, **bottom**: FEA).

The thermal strain and stress have been calculated by the FEA model based on the mapped CFD temperature results. The maximum thermal stress applied to the die was 1003.7 MPa. The structural analysis model was verified by observing the fracture location of the distributor, which showed the fastest breakage in the die. The location of crack initiation and the length of the fracture were measured. The highest thermal stress position and the area with the most notable change in thermal stress were identical to the fracture location of the distributor. In conclusion, it was confirmed that the actual thermal stress-induced failure could be predicted through the one-way coupled thermo-structural analysis. Figure 15 shows the die's thermal strain–stress distribution and crack locations.

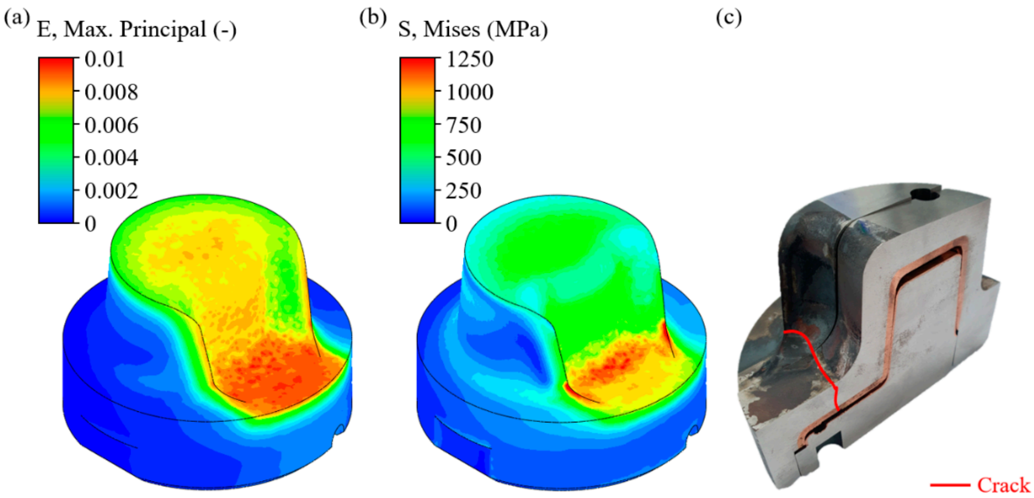

Figure 15. The structural analysis results and fractures caused by repeated thermal stress in the actual distributor. (**a**) Thermal strain distribution at 483 ssolution time. (**b**) Thermal stress distribution at 483 s solution time. (**c**) Crack location in the distributor.

3.3. Fatigue Life Prediction Based on the Semi-Empirical Model

A distributor with three flow paths was designed to identify the fatigue life due to different temperature gradients and to ensure the accuracy and wide usability of the prediction methodology. First, a distributor with a conformal cooling channel (CCC) that can quickly cool the heat from the molten metal by plating copper was proposed. In addition, the straight drilled channel (SDC) was applied, consisting of the AISI H13 material. Finally, a distributor was designed with no copper plating, although it was the same CCC as the first. The three distributor types are shown in detail in Figure 16.

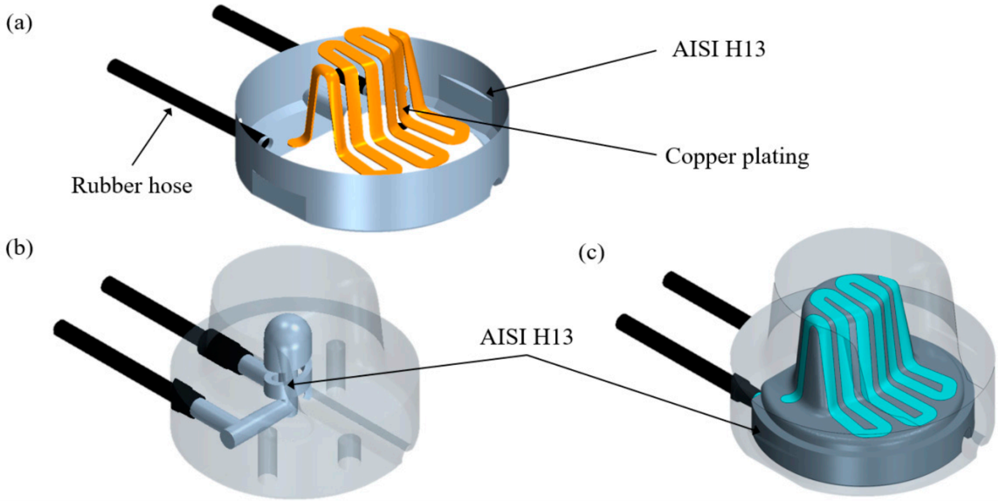

Figure 16. Various cooling channel models to validate the fatigue life prediction methodology. (**a**) Copper plating conformal cooling channel model (Cu CCC). (**b**) H13 straight drilled channel model (SDC). (**c**) AISI H13 conformal cooling channel model (H13 CCC).

Based on the validated numerical analysis model, the fatigue life of the HPDC die was estimated using von Mises stress and strain for each distributor design. The maximum and minimum stress–strain within one process cycle were extracted. The predicted fatigue lives were 7940; 37,280; and 51,270 cycles, respectively, as shown in Figure 17.

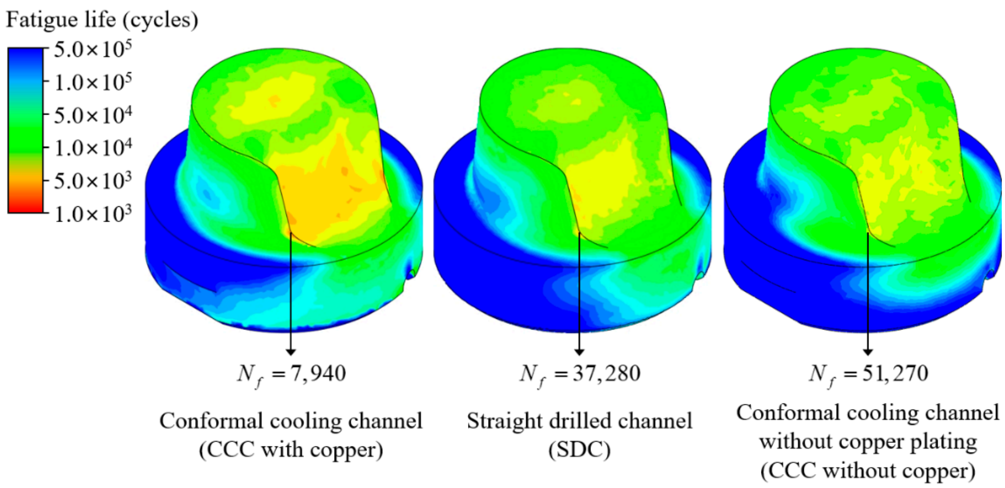

Figure 17. Fatigue life prediction results from three types of cooling channel.

4. Discussion

Static and cyclic mechanical properties of the AISI H13 hot work tool steel have been changed significantly depending on the temperature and triaxiality. Notably, as the temperature increases, the yield strength, and tensile strength decrease. Through this, it can be found that the damage received by the material is intensified as the temperature change continues. In addition, the higher the triaxiality, the fracture occurs quicker, making it difficult to predict the life of a die subjected to complex stress states.

In HPDC, the repeated thermal stress could be described through fatigue tests using notched specimens, ranging from room temperature (20 °C) to the molten metal temperature (500 °C). The semi-empirical model coefficient regressed through the experimental results showed a high correlation factor in combination with the one-way coupled numerical analysis technique. The advantage of the proposed methodology lies in the fact that it does not simplify the actual HPDC process to laboratory scale nor has the need to perform complex thermal stress experiments.

Unlike commercialized software, which focuses on the defects or the solidification of products, a one-way coupled thermofluid–structure analysis method with CFD and FEA is proposed. The CFD analysis model uses two measured temperatures. One is the temperature collected through a thermocouple in contact with molten metal and utilized to provide boundary conditions. The other is the temperature measured at the distributor using an infrared camera, which is adopted to verify the analysis model. As a result of the verification, the heat transfer coefficient derived through reverse engineering and the boundary conditions assigned to the analysis model were found to show high reliability.

The FEA model was used to investigate the combined thermal stress state of the test sample. The Johnson–Cook flow stress model, widely used to demonstrate the effect of temperature on the strain, was adopted to implement the behavior of temperature-dependent materials in the FEA. As a result of deriving the coefficient from a similar procedure for determining the model constant using experimental results according to temperature in the existing literature, the deformation of the material could be well represented. The load–displacement curves from the structural analysis were compared with the experimental results. The average deviation of the area integration was 2.27%, indicating good agreement. The results show that the implemented structural analytical model is reliable. Further, it is believed that using machine learning models such as artificial neural networks can consider thermal effects through the database without deriving material coefficients [42].

The die is subjected to a more severe temperature change with the increase in cooling efficiency. The fatigue life of die designs with three cooling channels was investigated to verify the presented fatigue life prediction procedure. Out of the three models, the CCC with copper plating had the highest cooling efficiency but also the lowest fatigue life. The SDC had lower cooling efficiency because less surface area was in contact with the die compared to the copper-plated cooling channel; however, the fatigue life increased as the temperature distribution was maintained uniformly. Despite its lower heat transfer efficiency, the AISI H13 CCC shows a fatigue life of nearly seven times that of the copper-plated channel. The results show that if the cooling channel design is solely focused on lowering the temperature of the die, it can lead to a distinct disadvantage in terms of the die replacement time.

In addition, the accuracy of the fatigue life prediction model has been confirmed by comparing the experimental and numerical analysis results of the copper-plated CCC die. Compared to the fact that actual die fracture occurs at 10,000 cycles on average, there was an error of about 20%. Given that the fracture occurs under low cycle fatigue, the proposed fatigue life prediction procedure is highly accurate and can be widely used in actual die design. Research on cooling channel design parameters that affect thermal stress by changing the temperature distribution of dies needs to be performed in the future.

5. Concluding Remarks

In this study, the thermally induced fatigue life of the AISI H13 hot work tool steel die was predicted. In addition, the effect of different cooling efficiency on the life of the HPDC die was analyzed. The results obtained are as follows:

1. The ultimate tensile strength decreases as the temperature increases, and it is the highest at 20 °C, decreasing by 9.1% at 300 °C and 15.5% at 500 °C.
2. A one-way coupled thermal–structure analysis model was developed. Compared with the IR camera measurement, the temperature results obtained from the CFD simulation varied by only 2.19%, verifying the thermofluid analysis boundary conditions.
3. The locations subjected to maximum thermal stress and thermal stress difference indicated by the FEA analysis results precisely matched the actual crack positions. In addition, the average deviation was 2.27%, showing high accuracy of structural analysis.

4. The energy-based semi-empirical fatigue life prediction model showed high accuracy with a correlation coefficient of 97.2%, showing high accuracy. In addition, the results differed by only 20% compared to 10,000 cycles: the low-cycle fatigue fracture of the copper-plated CCC die.
5. The CCC without copper had 6.46 times longer fatigue life than the copper-plated CCC, proving that the coolant passage with high cooling efficiency may not be an optimal die design.
6. The proposed fatigue life prediction methodology allows designers to predict fatigue life without manufacturing actual dies when designing HPDC dies.

Author Contributions: Conceptualization, N.K.; methodology, J.C. (Joeun Choi) and J.C. (Jongrak Choi); software, N.K. and N.H.; validation, J.C. (Joeun Choi) and J.C. (Jongrak Choi); formal analysis, J.C. (Joeun Choi); investigation, J.C. (Joeun Choi); resources, K.L.; data curation, J.C. (Joeun Choi); writing—original draft preparation, J.C. (Joeun Choi) and J.C. (Jongrak Choi); writing—review and editing, J.C. (Joeun Choi); visualization, J.C. (Joeun Choi); supervision, N.K.; project administration, N.K.; funding acquisition, K.L. All authors have read and agreed to the published version of the manuscript.

Funding: This research was funded by the Korea Institute for Advancement of Technology (KIAT), grant number P0017152, and the Material Component Technology Development Program, grant number 20013060.

Conflicts of Interest: The authors declare no conflict of interest.

References

1. Cleary, P.W.; Ha, J.; Prakash, M.; Nguyen, T. 3D SPH Flow Predictions and Validation for High Pressure Die Casting of Automotive Components. *Appl. Math. Model.* **2006**, *30*, 1406–1427. [CrossRef]
2. Lumley, R. The Development of High Strength and Ductility in High-Pressure Die-Cast Al-Si-Mg Alloys from Secondary Sources. *JOM* **2019**, *71*, 382–390. [CrossRef]
3. Kang, H.J.; Park, J.Y.; Choi, Y.S.; Cho, D.H. Influence of the Solution and Artificial Aging Treatments on the Microstructure and Mechanical Properties of Die-Cast Al–Si–Mg Alloys. *Metals* **2022**, *12*, 71. [CrossRef]
4. Bonollo, F.; Gramegna, N.; Timelli, G. High-Pressure Die-Casting: Contradictions and Challenges. *JOM* **2015**, *67*, 901–908. [CrossRef]
5. Casarotto, F.; Franke, A.J.; Franke, R. High-Pressure Die-Cast (HPDC) Aluminium Alloys for Automotive Applications. In *Advanced Materials in Automotive Engineering*; Woodhead Publishing: Cambridge, UK, 2012; pp. 109–149. [CrossRef]
6. Vicario, I.; Idoiaga, J.K.; Arratibel, E.; Erauskin, I.; Plaza, L.M.; Crespo, I.; Caballero, P. Development of HPDC Advanced Dies by Casting with Reinforced Tool Steels. *Int. J. Manuf. Eng.* **2015**, *2015*, 287986. [CrossRef]
7. Kovrigin, V.A.; Starokozhev, B.S.; Yurasov, S.A. Effect of Oxidizing Processes on Crazing of Die-Casting Molds. *Met. Sci. Heat Treat.* **1980**, *22*, 688–690. [CrossRef]
8. Persson, A.; Hogmark, S.; Bergström, J. Temperature Profiles and Conditions for Thermal Fatigue Cracking in Brass Die Casting Dies. *J. Mater. Process. Technol.* **2004**, *152*, 228–236. [CrossRef]
9. Persson, A.; Hogmark, S.; Bergström, J. Failure Modes in Field-Tested Brass Die Casting Dies. *J. Mater. Process. Technol.* **2004**, *148*, 108–118. [CrossRef]
10. Domkin, K.; Hattel, J.H.; Thorborg, J. Modeling of High Temperature- and Diffusion-Controlled Die Soldering in Aluminum High Pressure Die Casting. *J. Mater. Process. Technol.* **2009**, *209*, 4051–4061. [CrossRef]
11. Markežič, R.; Naglič, I.; Mole, N.; Šturm, R. Experimental and Numerical Analysis of Failures on a Die Insert for High Pressure Die Casting. *Eng. Fail. Anal.* **2019**, *95*, 171–180. [CrossRef]
12. Bouzakis, K.D.; Maliaris, G.; Tsouknidas, A. FEM Supported Semi-Solid High Pressure Die Casting Process Optimization Based on Rheological Properties by Isothermal Compression Tests at Thixo Temperatures Extracted. *Comput. Mater. Sci.* **2012**, *59*, 133–139. [CrossRef]
13. Dadić, Z.; Živković, D.; Čatipović, N.; Marinić-Kragić, I. Influence of Steel Preheat Temperature and Molten Casting Alloy $AlSi_9Cu_3$(Fe) Impact Speed on Wear of X38CrMoV5-1 Steel in High Pressure Die Casting Conditions. *Wear* **2019**, *424–425*, 15–22. [CrossRef]
14. Hattel, J.H.; Hansen, P.N. A 1-D Analytical Model for the Thermally Induced Stresses in the Mold Surface during Die Casting. *Appl. Math. Model.* **1994**, *18*, 550–559. [CrossRef]
15. Klobčar, D.; Tušek, J. Thermal Stresses in Aluminium Alloy Die Casting Dies. Comput. *Mater. Sci.* **2008**, *43*, 1147–1154. [CrossRef]
16. Lu, Y.; Ripplinger, K.; Huang, X.; Mao, Y.; Detwiler, D.; Luo, A.A. A New Fatigue Life Model for Thermally-Induced Cracking in H13 Steel Dies for Die Casting. *J. Mater. Process. Technol.* **2019**, *271*, 444–454. [CrossRef]

17. Li, Y.; Li, W.; Shao, J.; Deng, Y.; Kou, H.; Ma, J.; Zhang, X.; Zhang, X.; Chen, L.; Qu, Z. Modeling the Effects of Interfacial Properties on the Temperature Dependent Tensile Strength of Fiber Reinforced Polymer Composites. *Compos. Sci. Technol.* **2019**, *172*, 74–80. [CrossRef]
18. Statnik, E.S.; Uzun, F.; Lipovskikh, S.A.; Kan, Y.V.; Eleonsky, S.I.; Pisarev, V.S.; Somov, P.A.; Salimon, A.I.; Malakhova, Y.V.; Seferyan, A.G.; et al. Comparative Multi-modal, Multi-scale Residual Stress Evaluation in Slm 3d-printed Al-si-mg Alloy (Rs-300) Parts. *Metals* **2021**, *11*, 2064. [CrossRef]
19. Wolff, N.; Hohlweck, T.; Vroomen, U.; Bührig-Polaczek, A.; Hopmann, C. Development of an Experimental Setup to Investigate Influences on Component Distortion in Gravity Die Casting and a First Variation of Temperature Control Strategy. *Metals* **2021**, *11*, 2028. [CrossRef]
20. Ding, R.; Yang, H.; Li, S.; Hu, G.; Mo, J.; Chu, M.; Paddea, S.; Zhang, S.; Zhang, P.; Liu, Z.; et al. Failure Analysis of H13 Steel Die for High Pressure Die Casting Al Alloy. *Eng. Fail. Anal.* **2021**, *124*, 105330. [CrossRef]
21. Wei, C.; Ou, J.; Farhang Mehr, F.; Maijer, D.; Cockcroft, S.; Wang, X.; Lateng, A.; Chen, Z.; Zhu, Z. A Thermal-Stress Modelling Methodology in ABAQUS for Fundamentally Describing the Die/Casting Interface Behaviour in a Cyclic Permanent Die Casting Process. *J. Mater. Res. Technol.* **2021**, *15*, 5252–5264. [CrossRef]
22. Goodman, J. *Mechanics Applied to Engineering*; Longmans, Green & Co.: London, UK, 1919.
23. Smith, K.N.; Topper, T.; Watson, P. A Stress-Strain Function for the Fatigue of Metals. *J. Mater.* **1970**, *5*, 767–778.
24. Walker, K. The Effect of Stress Ratio during Crack Propagation and Fatigue for 2024-T3 and 7075-T6 Aluminum. In *Effects of Environment and Complex Load History on Fatigue Life*; ASTM International: West Conshohocken, PA, USA, 1970.
25. Coffin, L.F.J. A Study of the Effects of Cyclic Thermal Stresses on a Ductile Metal. *Trans. Am. Soc. Mech. Eng.* **1954**, *76*, 931–950. [CrossRef]
26. Manson, S.S. Fatigue: A Complex Subject—Some Simple Approximations. *Soc. Exp. Stress Anal.* **1964**, *15*, 193–226. [CrossRef]
27. Matsuishi, M.; Endo, T. Fatigue of Metals Subjected to Varying Stress. *Japan Soc. Mech. Eng.* **1968**, *68*, 37–40.
28. Choi, J.; Quagliato, L.; Shin, J.; Kim, N. Investigation on the Static and Cyclic Anisotropic Mechanical Behavior of Polychloroprene Rubber (CR) Reinforced with Tungsten Nano-Particles. *Eng. Fract. Mech.* **2020**, *235*, 107183. [CrossRef]
29. Choi, J.; Quagliato, L.; Lee, S.; Shin, J.; Kim, N. Multiaxial Fatigue Life Prediction of Polychloroprene Rubber (CR) Reinforced with Tungsten Nano-Particles Based on Semi-Empirical and Machine Learning Models. *Int. J. Fatigue* **2021**, *145*, 106136. [CrossRef]
30. Qian, D.; Ma, C.; Wang, F. The Effect of Flow Lines on the Mechanical Properties in Hot-Rolled Bearing Steel. *Metals* **2021**, *11*, 456. [CrossRef]
31. Lee, J.; Park, S.Y.; Choi, B.H. Evaluation of Fatigue Characteristics of Aluminum Alloys and Mechanical Components Using Extreme Value Statistics and C-Specimens. *Metals* **2021**, *11*, 1915. [CrossRef]
32. Tsuchiya, S.; Takahashi, K. Improving Fatigue Limit and Rendering Defects Harmless through Laser Peening in Additive-Manufactured Maraging Steel. *Metals* **2022**, *12*, 49. [CrossRef]
33. Ngeru, T.; Kurtulan, D.; Karkar, A.; Hanke, S. Mechanical Behaviour and Failure Mode of High Interstitially Alloyed Austenite under Combined Compression and Cyclic Torsion. *Metals* **2022**, *12*, 157. [CrossRef]
34. Wang, X.; Xiong, X.; Huang, K.; Ying, S.; Tang, M.; Qu, X.; Ji, W.; Qian, C.; Cai, Z. Effects of Deep Rolling on the Microstructure Modification and Fatigue Life of 35Cr2Ni4MoA Bolt Threads. *Metals* **2022**, *12*, 1224. [CrossRef]
35. Sun, T.; Xie, Y.; Pan, Y.; Zheng, Z.; Xie, C.; Huang, Z. Micromechanics-Based Low Cycle Fatigue Life Prediction Model of ECAPed Aluminum Alloy. *Metals* **2022**, *12*, 1127. [CrossRef]
36. Girisha, V.A.; Joshi, M.M.; Kirthan, L.J.; Bharatish, A.; Hegde, R. Thermal Fatigue Analysis of H13 Steel Die Adopted in Pressure-Die-Casting Process. *Sadhana Acad. Proc. Eng. Sci.* **2019**, *44*, 148. [CrossRef]
37. Sivertsen, S. Die Life Prediction Using High Pressure Die Casting Simulations. *Mater. Manuf.* **2020**, 1–41.
38. Mohammed, G.R.; Mubarak, E.M.; Abbas, B.H. Thermal Fatigue Model of Aluminium Alloy Die Casting H-13 Dies under Thermo-Mechanical Cycle. *Mechanika* **2021**, *27*, 385–391. [CrossRef]
39. Ucun, I.; Aslantas, K. Numerical Simulation of Orthogonal Machining Process Using Multilayer and Single-Layer Coated Tools. *Int. J. Adv. Manuf. Technol.* **2011**, *54*, 899–910. [CrossRef]
40. Priest, J.; Ghadbeigi, H.; Ayvar-Soberanis, S.; Liljerehn, A.; Way, M. A Modified Johnson-Cook Constitutive Model for Improved Thermal Softening Prediction of Machining Simulations in C45 Steel. *Procedia CIRP* **2022**, *108*, 106–111. [CrossRef]
41. Mohan, N.; Veerabhadrappa, K.; Basavaraja, J.S.; Suhas, B.G.; Kumar, R.S. Thermal Analysis on Ti-6AL-4V Tool Architecture Using Johnson–Cook Material Model. *Glob. Transit. Proc.* **2022**, *in press*. [CrossRef]
42. Deb, S.; Muraleedharan, A.; Immanuel, R.J.; Panigrahi, S.K.; Racineux, G.; Marya, S. Establishing Flow Stress Behaviour of Ti-6Al-4V Alloy and Development of Constitutive Models Using Johnson-Cook Method and Artificial Neural Network for Quasi-Static and Dynamic Loading. *Theor. Appl. Fract. Mech.* **2022**, *119*, 103338. [CrossRef]
43. *ASTM E8*; ASTM E8/E8M Standard Test Methods for Tension Testing of Metallic Materials. ASTM International: West Conshohocken, PA, USA, 2010; pp. 1–27. [CrossRef]
44. *ASTM E466*; Standard Practice for Conducting Force Controlled Constant Amplitude Axial Fatigue Tests of Metallic Materials. ASTM International: West Conshohocken, PA, USA, 2002; Volume 3, pp. 4–8. [CrossRef]